THE ASTROPHYSICAL JOURNAL, 974:262 (14pp), 2024 October 20 https://doi.org/10.3847/1538-4357/ad74fb

A Yebes W-band Line Survey towards an Unshocked Molecular Cloud of Supernova Remnant 3C 391: Evidence of Cosmic-Ray-Induced Chemistry

Tian-Yu Tu (涂天宇)[1], Prathap Rayalacheruvu[2,3], Liton Majumdar[2,3], Yang Chen (陈阳)[1,4], Ping Zhou (周平)[1,4], and Miguel Santander-García[5]

[1] School of Astronomy & Space Science, Nanjing University, 163 Xianlin Avenue, Nanjing 210023, People's Republic of China; ygchen@nju.edu.cn
[2] School of Earth and Planetary Sciences, National Institute of Science Education and Research, Jatni 752050, Odisha, India
[3] Homi Bhabha National Institute, Training School Complex, Anushaktinagar, Mumbai 400094, India
[4] Key Laboratory of Modern Astronomy and Astrophysics, Nanjing University, Ministry of Education, Nanjing 210023, People's Republic of China
[5] Observatorio Astronómico Nacional (OAN-IGN), Spain

Received 2024 April 13; revised 2024 August 20; accepted 2024 August 27; published 2024 October 16

Abstract

Cosmic rays (CRs) have strong influences on the chemistry of dense molecular clouds (MCs). To study the detailed chemistry induced by CRs, we conducted a Yebes W-band line survey towards an unshocked MC (which we named 3C391:NML) associated with supernova remnant 3C 391. We detected emission lines of 18 molecular species in total and estimated their column densities with local thermodynamic equilibrium (LTE) and non-LTE analysis. Using the abundance ratio $N(\mathrm{HCO^+})/N(\mathrm{CO})$ and an upper limit of $N(\mathrm{DCO^+})/N(\mathrm{HCO^+})$, we estimated that the CR ionization rate of 3C391:NML is $\zeta \gtrsim 2.7 \times 10^{-14}\,\mathrm{s^{-1}}$ with an analytic method. However, we caution against adopting this value because chemical equilibrium, which is a prerequisite of using the equations, is not necessarily reached in 3C391:NML. We observed lower $N(\mathrm{HCO^+})/N(\mathrm{HOC^+})$, higher $N(\mathrm{HCS^+})/N(\mathrm{CS})$, and higher $X(l\text{-}\mathrm{C_3H^+})$ by an order of magnitude in 3C391:NML than the typical values in quiescent dense MCs. We found that an enhanced CR ionization rate (of order $\sim 10^{-15}$ or $\sim 10^{-14}\,\mathrm{s^{-1}}$) is needed to reproduce the observation with a chemical model. This is higher than the values found in typical MCs by 2–3 orders of magnitude.

Unified Astronomy Thesaurus concepts: Cosmic rays (329); Chemical abundances (224); Molecular clouds (1072); Supernova remnants (1667); Abundance ratios (11)

1. Introduction

Supernova remnants (SNRs) are believed to be the prime accelerators of cosmic rays (CRs) in our Galaxy (F. A. Aharonian 2013). While high-energy CRs ($\gtrsim$280 MeV) can emit γ-rays through p–p interaction with molecular clouds (MCs), low-energy CRs act as the dominant source of ionization in MCs shielded from UV radiation (L. Spitzer 1978; M. Padovani et al. 2009). CR protons can ionize molecular hydrogen through

$$\mathrm{H_2} \longrightarrow \mathrm{H_2^+} + \mathrm{e^-} \tag{1}$$

followed by

$$\mathrm{H_2^+} + \mathrm{H_2} \longrightarrow \mathrm{H_3^+} + \mathrm{H}. \tag{2}$$

The $\mathrm{H_3^+}$ ion starts the process of the formation of polyatomic molecular species. The CR ionization rate per $\mathrm{H_2}$ molecule, defined as the rate coefficient of reaction (1) (here we do not include the effect of secondary electrons), is an important parameter to quantify the ionization effect of CRs in a certain astrophysical environment. Chemical effects of CRs on MCs are not limited to the ionization of $\mathrm{H_2}$. CRs can also drive the transition of $\mathrm{CO} \rightarrow \mathrm{C} \rightarrow \mathrm{C^+}$ (T. G. Bisbas et al. 2017). Other chemical effects of CRs include CR-induced non-thermal desorption (T. I. Hasegawa & E. Herbst 1993), CR-induced UV photons (S. S. Prasad & S. P. Tarafdar 1983; A. Sternberg et al. 1987), grain sputtering (V. Wakelam et al. 2021; A. Paulive et al. 2022), radiolysis (C. N. Shingledecker et al. 2018; A. Paulive et al. 2021), etc.

SNRs provide an ideal environment for us to study how CRs affect the chemistry in MCs. Observations have revealed an enhanced CR ionization rate ($\sim 10^{-15}\,\mathrm{s^{-1}}$ compared with typical values $\sim 10^{-17}\,\mathrm{s^{-1}}$; A. E. Glassgold & W. D. Langer 1974) in dense MCs associated with SNRs W51C (C. Ceccarelli et al. 2011), W28 (S. Vaupré et al. 2014; T.-y. Tu et al. 2024), W44 (G. Cosentino et al. 2019), and W49B (P. Zhou et al. 2022). All of these SNRs are interacting with MCs and exhibit hadronic γ-ray emission that originates from the collision between the high-energy CR protons and H nuclei in the MCs. However, the detailed behavior of CR chemistry is seldom studied in the environment of an SNR.

SNR 3C 391 is among the prototype SNRs interacting with MCs (B. Jiang et al. 2010) as evidenced by 1720 MHz OH masers (D. A. Frail et al. 1996), broadened molecular lines (W. T. Reach & J. Rho 1999, hereafter RR99), and infrared emission from molecules, atoms, and ions (e.g., W. T. Reach & J. Rho 1996, 1998, 2000). The OH masers suggest an enhanced CR ionization rate (A. V. Nesterenok 2022). A marginal detection of the 6.4 keV Fe I Kα line was reported by T. Sato et al. (2014), which is likely the fluorescence produced by interaction between low-energy CRs and dense gas. In the γ-ray band, GeV emission has been detected with Fermi (T. Ergin et al. 2014), which also favors an enhanced CR ionization rate. In addition, an unshocked MC dominated by narrow molecular lines is found outside the shocked cloud (see Figure 6 of RR99 and Figure 1), which provides an excellent site to study the chemical effect of CRs free from the disturbance of the SNR shock wave. Hereafter we refer to this region as 3C391:NML (narrow molecular line), following the nomenclature of RR99,

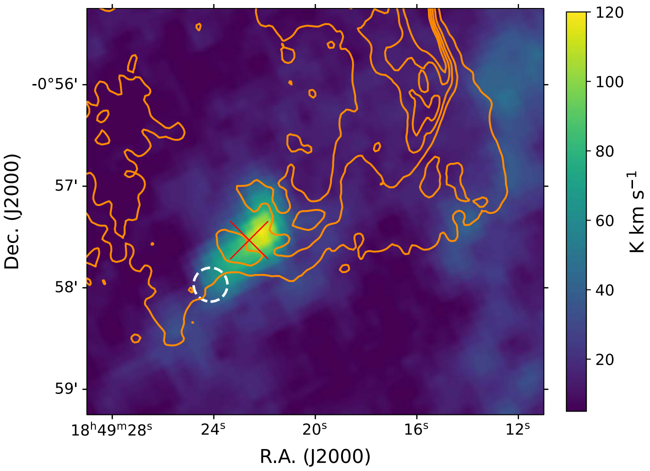

Figure 1. Integrated intensity map of the ^{12}CO $J=3$–2 line between +100 and +110 km s^{-1} toward the southwestern part of SNR 3C 391, overlaid with orange contours of 1.4 GHz radio continuum (levels are 4, 12, 20, 28, and 36 mJy beam^{-1}). The red cross shows the 1720 MHz OH maser reported by D. A. Frail et al. (1996). The dashed white circle delineates the 3C391:NML region we observed.

who named the shocked region around the southern 1720 MHz OH maser as 3C391:BML (broad molecular line).

In this paper, we present a new W-band (71.5–90 GHz) molecular line survey with the Yebes 40 m radio telescope toward 3C391:NML, aiming at enlarging the sample of SNRs exhibiting an enhanced CR ionization rate and investigating the detailed CR chemistry. The paper is organized as follows. We describe the new observation and the archival data in Section 2, and present the observational results in Section 3. In Section 4, we estimate the column densities of detected molecular species, discuss how CRs affect the observed abundances and abundance ratios, and present the result of our chemical simulation. The conclusions are summarized in Section 5.

2. Observations

2.1. Yebes 40 m Observation

We carried out a new pointing observation with the Yebes 40 m radio telescope (PI: Tian-Yu Tu, project code: 23A021) toward 3C391:NML ($\alpha_{\rm J2000} = 18^{\rm h}49^{\rm m}24\overset{\rm s}{.}13$, $\delta_{\rm J2000} = -0°57'58\overset{''}{.}17$, see the dashed white circle in Figure 1), which was found by RR99 with narrow-line CS $J=2-1$ emission. Position-switching mode was adopted throughout the observation with the reference point at $\alpha_{\rm J2000} = 18^{\rm h}52^{\rm m}08^{\rm s}$, $\delta_{\rm J2000} = -1°09'17''$. The spectral coverage ranged from 71.5 to 90 GHz. The half-power beam width of the telescope was in the range ∼20″–24″. The data were smoothed to a velocity channel width of 0.2km s^{-1}, and the resulting sensitivity measured in main beam temperature ($T_{\rm mb}$) is ≈12–15 mK depending on the frequency. The raw data were reduced with the GILDAS/CLASS package.[6]

2.2. Other Archival Data

We used other archival data to support our analysis. We obtained ^{12}CO and ^{13}CO $J=1$–0 data from the FUGIN (FOREST Unbiased Galactic Plane Imaging Survey with the Nobeyama 45 m telescope) project (T. Umemoto et al. 2017). The angular resolutions are 20″ for ^{12}CO and 21″ for ^{13}CO, and the sensitivity estimated in $T_{\rm mb}$ is ∼1–3 K at a velocity channel width of 0.65 km s^{-1}.

We also obtained ^{12}CO $J=3$–2 data from the ^{12}CO (3–2) High-Resolution Survey (COHRS) project (G. Park et al. 2023). The angular resolution is 16$\overset{''}{.}$6 and the sensitivity measured in $T_{\rm A}^{*}$ is ∼1 K at a velocity channel width of 0.635 km s^{-1}. The antenna temperature was converted to $T_{\rm mb}$ with a main beam efficiency of 0.61. We smoothed the data to an angular resolution of 20″, which is similar to the beam of the FUGIN data and our Yebes data.

A supplementary Very Large Array 1.4 GHz radio continuum map was taken from the SNRcat[7] (G. Ferrand & S. Safi-Harb 2012). All the processed data were further analyzed with Python packages Astropy (Astropy Collaboration et al. 2018, 2022) and Spectral-cube (A. Ginsburg et al. 2015). The data cubes of the CO isotopes were reprojected with the Montage[8] package. We visualized the data with Python package Matplotlib.[9]

3. Results

In Figures 2 and 3 we display the spectra of all the molecular lines detected by the Yebes 40 m observation, as well as the spectra of three CO lines and the non-detection of the DCO$^+$ $J=1$–0 line. We detected 18 species (including isotopes) in total, some of which are seldom studied in the environment of SNRs.

Also shown in Figures 2 and 3 are the results (multi-) Gaussian fitting to the spectra. All of the detected species show narrow line emission centered at $V_{\rm LSR} \approx 105.5$ km s^{-1}, consistent with the results of RR99. The fitted $T_{\rm peak}$ and FWHM of the narrow components are summarized in Table 2.

We find three components in the spectrum of HCO$^+$ (see Figure 2): a narrow line centered at 105.4 km s^{-1}, a moderately broadened component centered at 102.5 km s^{-1} with an FWHM of 9.7 km s^{-1}, and a very broad component centered at 103.4 km s^{-1} with an FWHM of 34.8 km s^{-1}. The moderately broadened component has been reported by RR99, but the broadest component is detected for the first time. These two broadened components may be the results of the shock of the SNR propagating into different layers of 3C391:NML. In the outer layer, the velocity of the shock is high, resulting in a large line-width, while the opposite is true when the shock wave goes deeper into the cloud. Detailed analysis of the shocked components is beyond the scope of this study.

A similar line profile is also found in the spectra of the HCN $J=1$–0 line, but two peaks can be seen on the blue and red sides of the main peak. These are the hyperfine structures (HFS) located at −7.1 km s^{-1} and +4.9 km s^{-1} relative to the main component. Spectra consisting of two components—a narrow one and a moderately broadened one—were detected in ^{12}CO $J=3$–2, H$_2$CO $1_{0,1}$–$0_{0,0}$, H^{13}CN $J=1$–0, four lines of C$_2$H, and two lines of c-C$_3$H$_2$.

Hereafter, we mainly focus on the narrow component because it is supposed to be free from the disturbance of the SNR shock wave. We note that RR99 found $T_{\rm peak}$ of the narrow component of HCO$^+$ to be 1.0 K, which is smaller than the fitted value shown in Table 2. This is because the beam size of their observation is 27″, which is larger than our 20″ beam. Using these values, we can

---

[6] https://www.iram.fr/IRAMFR/GILDAS/

[7] http://snrcat.physics.umanitoba.ca

[8] http://montage.ipac.caltech.edu/

[9] https://matplotlib.org/

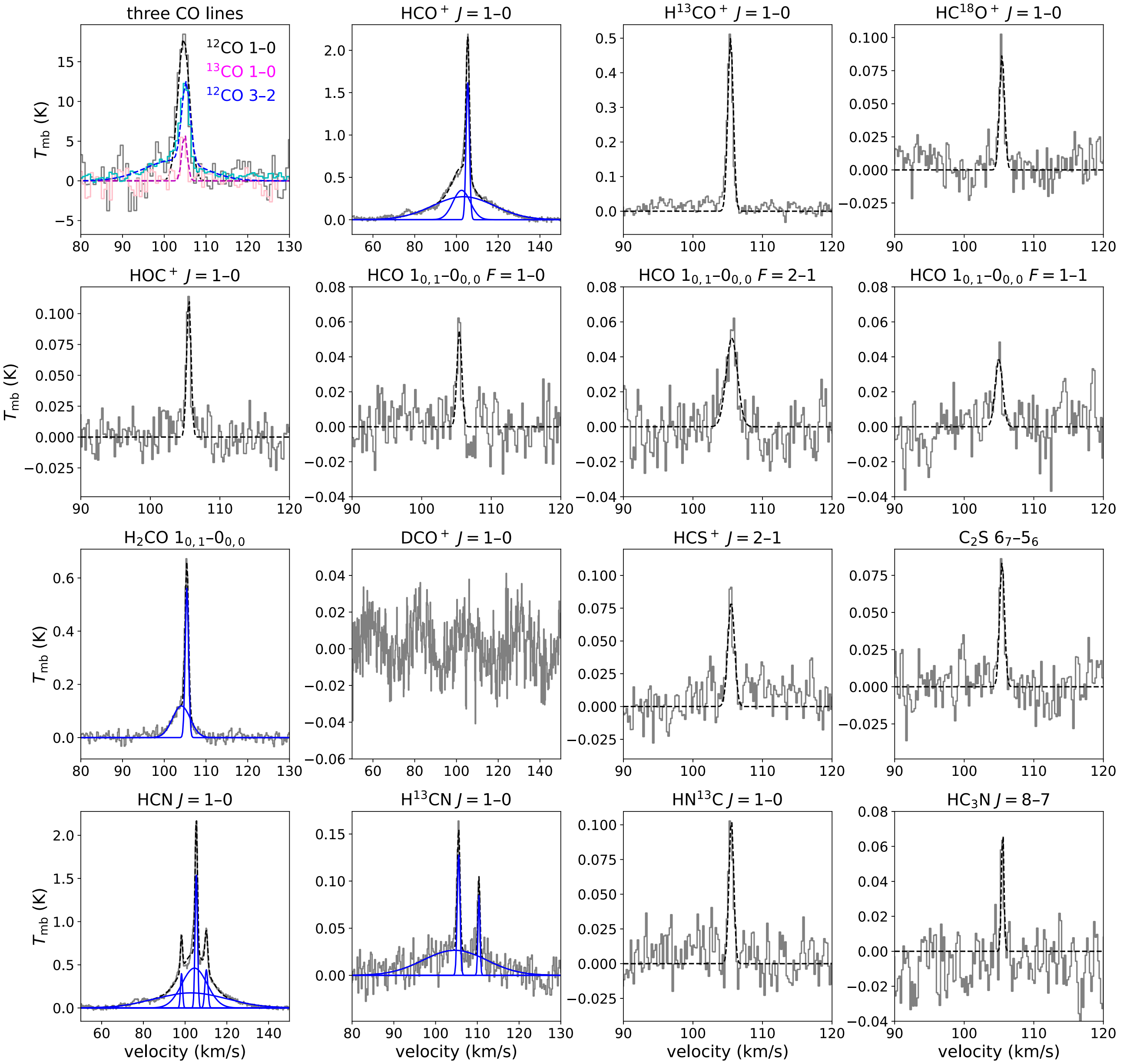

Figure 2. The spectra of molecular lines detected by the Yebes 40 m observation, as well as the spectra of three CO lines and the non-detection of the DCO$^+$ $J = 1$–0 line. For the CO lines, the solid gray, pink, and cyan lines show the ^{12}CO $J = 1$–0, ^{13}CO $J = 1$–0, and ^{12}CO $J = 3$–2 lines, respectively, while the dashed black, magenta, and blue lines show the results of (multi-)Gaussian fitting to the ^{12}CO $J = 1$–0, ^{13}CO $J = 1$–0, and ^{12}CO $J = 3$–2 lines, respectively. For other molecular transitions, the gray lines show the observed spectra, the black lines show the fitting results, and the blue lines show the components if multi-Gaussian fitting is adopted. The ranges of the local-standard-of-rest (LSR) velocity are adjusted for better visualization.

estimate that the angular size of the MC emitting the narrow lines is $\approx 27'' \times (1.0/1.62)^{0.5} \approx 21''$. Therefore, we assume the beam filling factor is unity in the following discussions.

4. Discussion

4.1. Estimation of Molecular Column Density

4.1.1. Non-LTE Estimation

To estimate the column densities of different molecular species of the unshocked component, we first use SpectralRadex,[10] which is a Python wrapper of the radiative transfer code, RADEX (F. F. S. van der Tak et al. 2007), to present non-LTE (local thermodynamic equilibrium) analysis. The collisional coefficients are taken from LAMDA[11] (Leiden Atomic and Molecular Database; F. van der Tak et al. 2020). The geometry of the emitting object is chosen to be a sphere. We assume a kinetic temperature $T \approx 20$ K, consistent with the value adopted by RR99 and the temperature estimated from the line ratio $I(\mathrm{H^{13}CN})/I(\mathrm{HN^{13}C})$ (A. G. Pazukhin et al. 2022), which is $\approx$23 K in our case. The analysis is conducted with CO, o-c-C$_3$H$_2$, and CS. The data of CS emission lines are obtained from the results of RR99. We run a grid of density ($n_{\mathrm{H_2}}$) and column density (N) of specific molecular species and find the best-fit values for each species. The results are shown in Figure 4 and Table 1.

---

[10] https://spectralradex.readthedocs.io/en/latest/

[11] https://home.strw.leidenuniv.nl/~moldata/

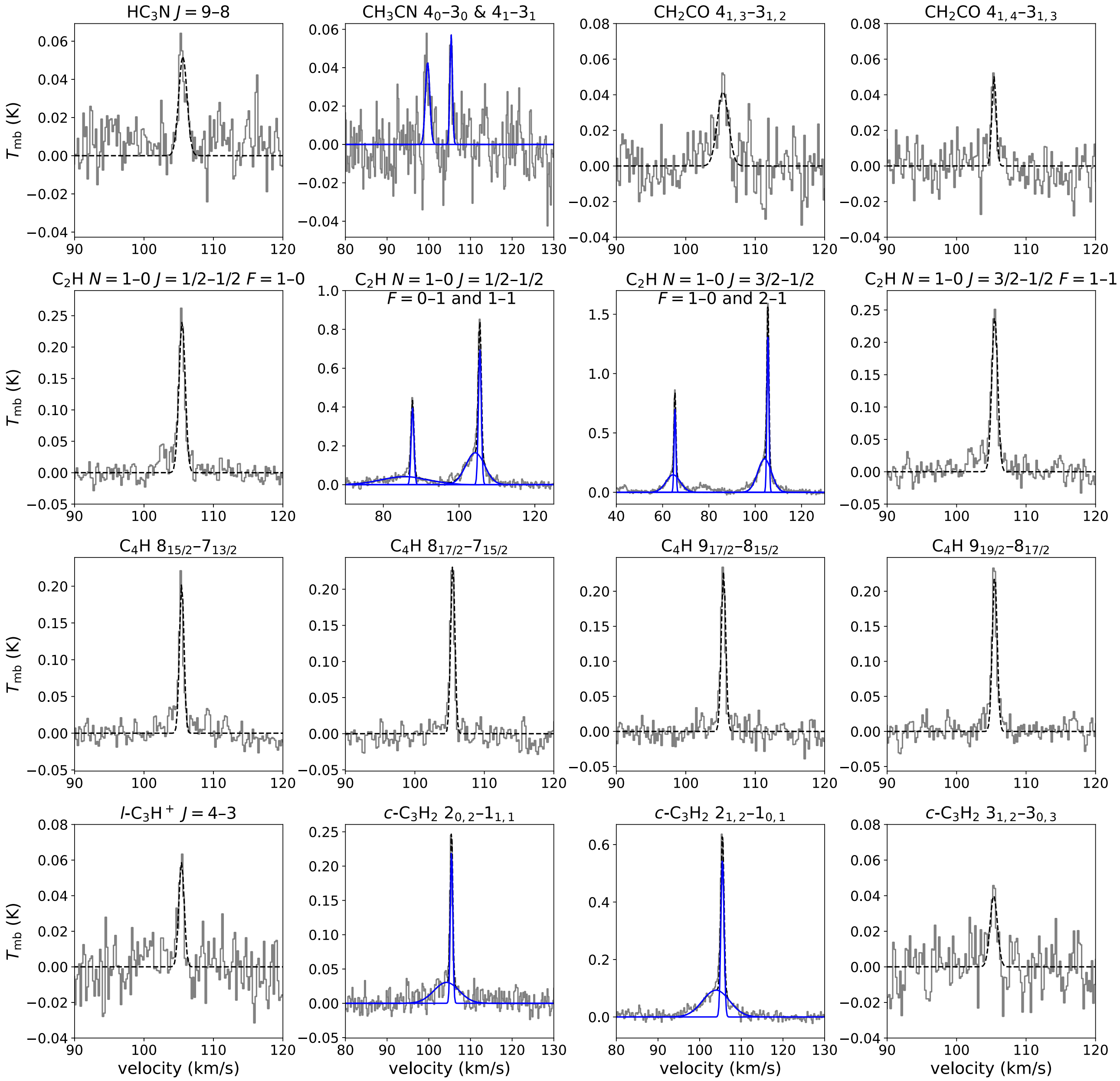

Figure 3. Same as Figure 2 but for different species.

For CO, we use the ^{12}CO 1–0, ^{13}CO 1–0, and ^{12}CO 3–2 lines for the analysis, and we fit the ratios $T_{\mathrm{mb}}(^{12}\mathrm{CO}\ 3\text{–}2)/T_{\mathrm{mb}}(^{12}\mathrm{CO}\ 1\text{–}0)$ and $T_{\mathrm{mb}}(^{12}\mathrm{CO}\ 3\text{–}2)/T_{\mathrm{mb}}(^{13}\mathrm{CO}\ 1\text{–}0)$. We assume $N(^{12}\mathrm{CO})/N(^{13}\mathrm{CO}) = 45$ in our calculation (S. N. Milam et al. 2005). The best-fit values, marked by the intersection point of the two solid lines in the upper left panel of Figure 4, are $N(^{12}\mathrm{CO}) \sim 3.7 \times 10^{17}\ \mathrm{cm}^{-2}$ and $n_{\mathrm{H}_2} \sim 1.4 \times 10^3\ \mathrm{cm}^{-3}$. We note that there is parameter degeneracy in our fitting, so the values are just a rough estimation.

For o-c-C_3H_2, we use the o-c-C_3H_2 $3_{1,2}$–$3_{0,3}$ and $2_{1,2}$–$1_{0,1}$ lines, and fit the $T_{\mathrm{mb}}(3_{1,2}\text{–}3_{0,3})/T_{\mathrm{mb}}(2_{1,2}\text{–}1_{0,1})$ ratio and $T_{\mathrm{mb}}(2_{1,2}\text{–}1_{0,1})$. The best-fit values are $N(o\text{-}c\text{-}C_3H_2) \sim 2.0 \times 10^{12}\ \mathrm{cm}^{-2}$ and $n_{\mathrm{H}_2} \sim 2.4 \times 10^5\ \mathrm{cm}^{-3}$.

For CS, we fit $T_{\mathrm{mb}}(\mathrm{CS}\ 3\text{–}2)/T_{\mathrm{mb}}(\mathrm{CS}\ 2\text{–}1)$ and $T_{\mathrm{mb}}(\mathrm{CS}\ 2\text{–}1)$, and use the non-detection of CS 5–4 reported by RR99 as an upper limit. The best-fit values are $N(\mathrm{CS}) \sim 3.9 \times 10^{12}\ \mathrm{cm}^{-2}$ and $n_{\mathrm{H}_2} \sim 1.9 \times 10^5\ \mathrm{cm}^{-3}$. We also show the fitting results of CS assuming $T = 40$ K in the lower right panel of Figure 4. The results shows that the kinetic temperature of 3C391:NML should not be much higher than 40 K, otherwise the CS 5–4 line should have been detected. The CS lines set an upper limit for the kinetic temperature T. We also note that although the kinetic temperatures are different, the best-fit $N(\mathrm{CS})$ does not change significantly, and the variation of the corresponding excitation temperature of the CS 2–1 line ($\approx$10 K) is also not prominent. This excitation temperature will be used to conduct LTE analysis for the other species in the following section.

The densities estimated with the o-c-C_3H_2 and CS lines are respectively similar to and higher than that estimated with CO. This is not surprising because the critical densities are $\sim 10^6\ \mathrm{cm}^{-3}$ for the o-c-C_3H_2 and CS lines, but $\sim 10^3$–$10^4\ \mathrm{cm}^{-3}$ for the CO lines, which means that o-c-C_3H_2 and CS trace a denser part of the MC than CO.

For other molecular species, non-LTE analysis is not available. We use LTE analysis to estimate their column densities.

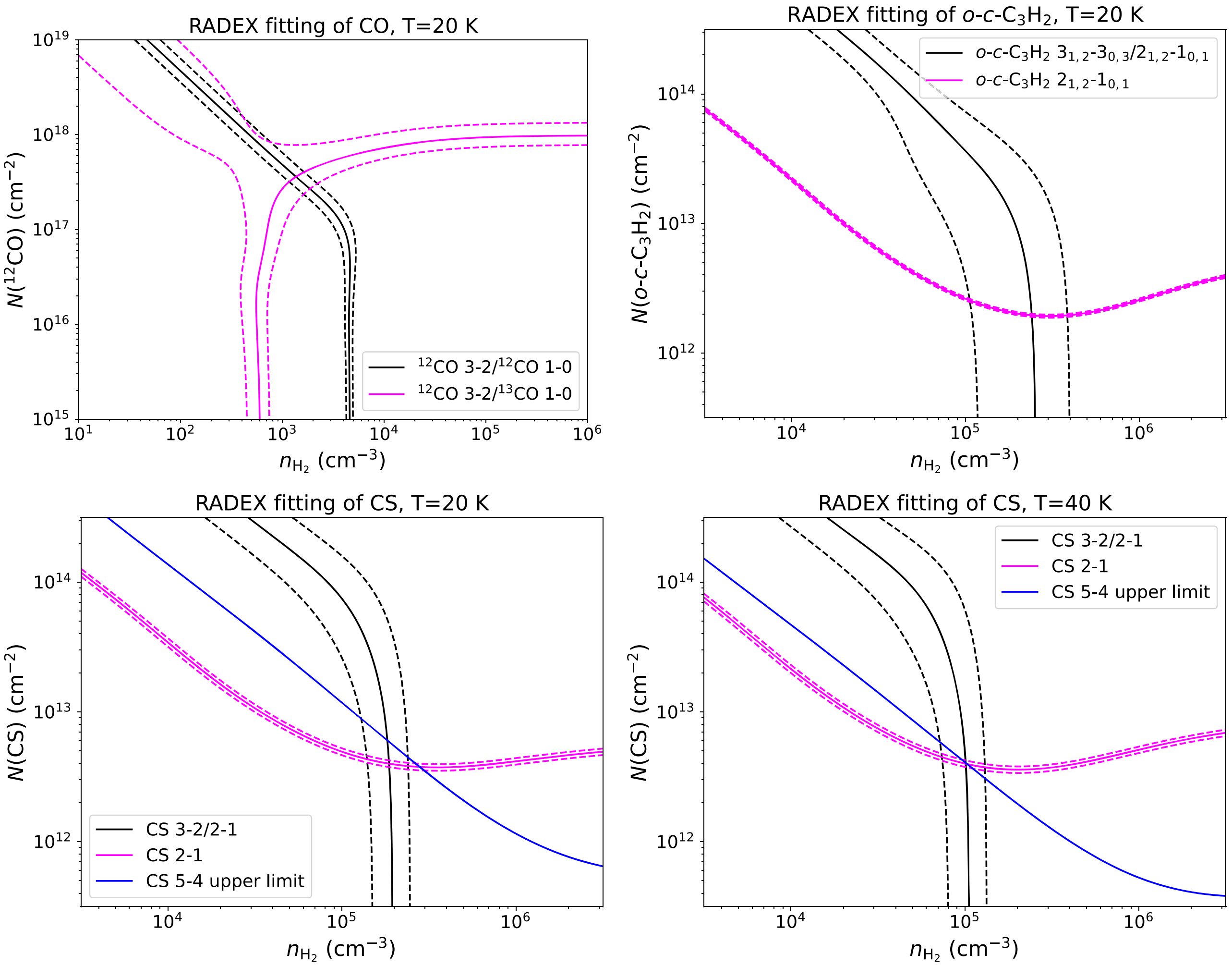

Figure 4. Results of the non-LTE analysis with SpectralRadex. The solid contours show the observed $T_{\rm mb}$ or $T_{\rm mb}$ ratios of lines, while the dashed lines are the estimated uncertainties of the observed values. Upper left: results of CO with $T = 20$ K. The black contours show ^{12}CO 3–2/^{12}CO 1–0. The magenta contours show ^{12}CO 3–2/^{13}CO 1–0. Upper right: results of o-c-C$_3$H$_2$ with $T = 20$ K. The black contours show o-c-C$_3$H$_2$ $3_{1,2}$–$3_{0,3}$/$2_{1,2}$–$1_{0,1}$. The magenta contours show the $2_{1,2}$–$1_{0,1}$ line. Lower left: results of CS with $T = 20$ K. The black contours show CS 3–2/2–1. The magenta contours show CS 2–1. The blue contour shows the upper limit of CS 5–4. Lower right: same as the lower left panel but for $T = 40$ K.

Table 1
Results of Non-LTE Analysis of CO, o-c-C$_3$H$_2$, and CS Lines

Species	Column Density (cm^{-2})	$n_{\rm H2}$ (cm^{-3})
CO	$\sim 3.7 \times 10^{17}$	$\sim 1.4 \times 10^{3}$
o-c-C$_3$H$_2$	$\sim 2.0 \times 10^{12}$	$\sim 2.4 \times 10^{5}$
CS (20 K)	$\sim 3.9 \times 10^{12}$	$\sim 1.9 \times 10^{5}$
CS (40 K)	$\sim 3.9 \times 10^{12}$	$\sim 1.0 \times 10^{5}$

4.1.2. LTE Estimation

We assume LTE condition for the molecular species other than CO, o-c-C$_3$H$_2$, and CS analyzed above. Assuming the lines to be optically thin, we obtain the column densities through (Equation C1 in X. C. Liu et al. 2021)

$$N = \frac{3k}{8\pi^3\nu}\frac{Q_{\rm rot}\exp(E_{\rm u}/kT_{\rm ex})}{S\mu^2} \times \frac{J_\nu(T_{\rm ex})}{J_\nu(T_{\rm ex}) - J_\nu(T_{\rm bg})}\int T_{\rm mb}\,dv, \quad (3)$$

where $Q_{\rm rot}$ is the partition function, $E_{\rm u}$ is the energy of the upper level, $T_{\rm ex}$ is the excitation temperature, S is the line strength, μ is the dipole moment, $T_{\rm bg} = 2.73$ K is the background temperature, and $J_\nu(T)$ is defined by $J_\nu(T) = (h\nu/k)/(\exp(h\nu/kT) - 1)$. We adopt $Q_{\rm rot}$, $E_{\rm u}$, and $S\mu^2$ from Splatalogue.[12] The data of HCO are extracted from the JPL database,[13] while other data are from the CDMS database.[14]

We use two values of $T_{\rm ex}$ (5 and 10 K) to estimate the column density for each molecular species, which is tabulated in Table 2. $T_{\rm ex}$ is calculated with the following two methods. (1) The optical depth of HCO$^+$ can be obtained by solving

$$\frac{1 - e^{-\tau}}{1 - e^{-\tau/327}} = \frac{W({\rm HCO^+})}{W({\rm HC^{18}O^+})}, \quad (4)$$

where W is the integrated intensity and we assume $N({\rm HCO^+})/N({\rm HC^{18}O^+}) \approx N(^{16}{\rm O})/N(^{18}{\rm O}) \approx 327$ (Y. T. Yan et al. 2023) considering the galactocentric distance of 3C 391 is $\approx$4.4 kpc (S. Ranasinghe & D. Leahy 2022). We get $\tau \approx 8$, which is high enough for us to estimate the excitation

---

[12] https://splatalogue.online/

[13] https://spec.jpl.nasa.gov/

[14] https://cdms.astro.uni-koeln.de/

Table 2

Results from Gaussian Fitting of the Narrow Line Components of All Detected Lines in the Yebes 40 m Observation, as well as the Column Densities of Molecular Species

Species	Transition	Frequency (MHz)	$T_{\rm peak}$ (K)	FWHM (km s^{-1})	$N(T_{\rm ex} = 5\ {\rm K})$[a] ($cm^{-2}$)	$N(T_{\rm ex} = 10\ {\rm K})$[a] ($cm^{-2}$)
HCO^+	1–0	89,188.525	1.62	1.87	3.3(13) for HCO^+[b]	2.9(13) for HCO^+[b]
$H^{13}CO^+$	1–0	86,754.288	0.50	0.93		
$HC^{18}O^+$	1–0	85,162.223	0.087	0.74		
DCO^+	1–0	72,039.312	<0.045 [c]	⋯	<7.7(10)	<7.1(10)
HCN	1–0 $F = 0–1$	88,633.936	0.40	1.16	1.5(13) for HCN[d]	1.3(13) for HCN[d]
	1–0 $F = 2–1$	88,631.847	1.54	1.36		
	1–0 $F = 1–1$	88,630.416	0.44	1.63		
$H^{13}CN$	1–0 $F = 1–1$	86,338.737	0.085	0.56		
	1–0 $F = 2–1$	86,340.176	0.13	0.77		
$HN^{13}C$	1–0	87,090.859	0.10	0.81	1.8(11)	1.6(11)
HOC^+	1–0	89,487.414	0.11	0.73	2.1(11)	1.9(11)
HCO	$1_{0,1}–0_{0,0}$					
	$J, F = 3/2, 1–1/2, 0$	86,708.35	0.056	0.80	1.2(12)	2.0(12)
	$J, F = 3/2, 2–1/2, 1$	86,670.82	0.050	1.96	1.6(12)	2.5(12)
	$J, F = 1/2, 1–1/2, 1$	86,777.43	0.038	1.28	1.4(12)	2.2(12)
H_2CO	$1_{0,1}–0_{0,0}$	72,837.951	0.57	0.93	3.5(12)	6.3(12)
HCS^+	2–1	85,347.869	0.080	1.13	6.9(11)	5.3(11)
HC_3N	8–7	72,783.818	0.075	0.41	5.9(11)	1.7(11)
	9–8	81,881.463	0.052	1.40	2.4(12)	5.5(11)
C_2H	$N = 1–0$				1.9(14)	1.8(14)
	$J, F = 1/2, 1–1/2, 0$	87,446.512	0.24	1.08		
	$J, F = 1/2, 0–1/2, 1$	87,407.165	0.39	0.88		
	$J, F = 1/2, 1–1/2, 1$	87,402.004	0.70	0.89		
	$J, F = 3/2, 1–1/2, 0$	87,328.624	0.70	0.92		
	$J, F = 3/2, 2–1/2, 1$	87,316.925	1.34	0.99		
	$J, F = 3/2, 1–1/2, 1$	87,284.156	0.24	1.01		
C_2S	$6_7–5_6$	81,505.208	0.086	0.80	1.6(12)	8.8(11)
C_4H	$8_{17/2}–7_{15/2}$	76,117.43	0.23	0.73	4.3(13)	1.2(13)
	$8_{15/2}–7_{13/2}$	76,156.02	0.20	0.77		
	$9_{19/2}–8_{17/2}$	85,634.00	0.22	0.81	8.3(13)	1.6(13)
	$9_{17/2}–8_{15/2}$	85,672.57	0.23	0.76		
l-C_3H^+	4–3	89,957.625	0.067	0.75	3.5(11)	1.8(11)
o-c-C_3H_2	$3_{1,2}–3_{0,3}$	82,966.201	0.041	1.22	2.0(12)[e]	
	$2_{1,2}–1_{0,1}$	85,338.906	0.56	0.87		
p-c-C_3H_2	$2_{0,2}–1_{1,1}$	82,093.555	0.23	0.68	3.7(12)	4.1(12)
CH_2CO	$4_{1,3}–3_{1,2}$	81,586.229	0.041	1.92	1.7(13)	4.8(12)
	$4_{1,4}–3_{1,3}$	80,076.644	0.051	0.74	8.1(12)	2.3(12)
CH_3CN	$4_1–3_1$	73,588.799	0.056	0.71	9.4(11)	3.4(11)
	$4_0–3_0$	73,590.217	0.044	1.19	2.8(11)	2.1(11)

Notes.

[a] $m(n)$ means $m \times 10^n$.

[b] The column density of HCO^+ is estimated from $HC^{18}O^+$ assuming $N(HCO^+)/N(HC^{18}O^+) \approx N(^{16}O)/N(^{18}O) \approx 327$ (Y. T. Yan et al. 2023).

[c] DCO^+ is not detected, so we use the 3σ value as an upper limit.

[d] The column density of HCN is estimated from $H^{13}CN$ assuming $N(HCN)/N(H^{13}CN) \approx N(12C)/N(13C) \approx 45$ (S. N. Milam et al. 2005).

[e] The column density of o-c-C_3H_2 is estimated with a non-LTE method (see Section 4.1.1).

temperature of HCO^+ using (J. G. Mangum & Y. L. Shirley 2015)

$$T_{\rm ex} = \frac{h\nu/k}{\ln\left(1 + \frac{h\nu/k}{T_{\rm peak}/f + J_\nu(T_{\rm bg})}\right)}. \quad (5)$$

Then we get $T_{\rm ex} = 5$ K for HCO^+. We adopt this value as a first estimation of $T_{\rm ex}$. (2) According to the results of RADEX (in Section 4.1.1), the excitation temperature of the CS 2–1 line is ≈10 K. We adopt this value as the second estimation of $T_{\rm ex}$.

Equation (3) only applies when the transition is optically thin, which, however, is not necessarily the case in some of the detected lines. To minimize the influence of finite optical depth, we use the emission from rarer isotopes or the HFS to calculate the column density when isotopes or HFS are detected. Specifically, we use $HC^{18}O^+$ to calculate $N(HCO^+)$, $H^{13}CN$ for N(HCN), and C_2H $N = 1$–0 J, $F = 3/2$, 1–1/2, 1 for $N(C_2H)$. For C_4H, the results estimated with the two 8–7 lines (or the two 9–8 lines) are similar, but there is a significant difference between the values estimated with one 8–7 and one 9–8 line. For HCO, HC_3N, CH_2CO, and CH_3CN, although multiple transitions are detected, we calculate the column densities with all detected transitions because they are rather weak and the results are different.

As seen in Table 2, for most species, the column densities estimated with the two different $T_{\rm ex}$ are consistent within a factor of 2, except for HC_3N, C_4H, CH_2CO, and CH_3CN. For HC_3N, CH_2CO, and CH_3CN, there is also a non-negligible difference between the estimated column densities with different transitions, probably because the lines are rather weak and the relative uncertainty is high.

4.2. Relation between the Observed Molecular Abundances and CR Chemistry

In Section 4.1.1, we obtained $N(^{12}CO) \sim 3.7 \times 10^{17}$ cm^{-2}. Assuming $N(H_2) \approx 7 \times 10^5 N(^{13}CO)$ (M. A. Frerking et al. 1982), we obtain $N(H_2) \sim 5.8 \times 10^{21}$ cm^{-2}. We will use this value to estimate the molecular abundance relative to H_2.

4.2.1. Estimation of CR Ionization Rate with an Analytic Method

The abundance ratios $R_{\rm D} = N(DCO^+)/N(HCO^+)$ and $R_{\rm H} = N(HCO^+)/N$(CO) have been used to estimate the CR ionization rate in MCs (P. Caselli et al. 1998; C. Ceccarelli et al. 2011; S. Vaupré et al. 2014). Assuming the chemistry of 3C391:NML has reached equilibrium and the temperature is low (≪220 K), the CR ionization ζ can be calculated simply with (S. Vaupré et al. 2014)

$$\frac{\zeta}{n_{\rm H}} = \frac{\beta'}{k_{\rm H}}(2\beta x_{\rm e} + \delta)R_{\rm H}x_{\rm e},$$
$$x_{\rm e} = \left(\frac{k_{\rm f}\, x({\rm HD})}{3R_{\rm D}} - \delta\right)\frac{1}{k_{\rm e}} \quad (6)$$

where $x_{\rm e}$ is the ionization fraction in the MC, x(HD) is the abundance of HD relative to H, and $k_{\rm f}$, δ, β, and β' are rate coefficients of chemical reactions listed in Table A.1 of S. Vaupré et al. (2014). These equations allow us to set a lower limit for ζ even though DCO^+ is not detected. Assuming $x({\rm HD}) = 1.6 \times 10^{-5}$ (J. L. Linsky et al. 2006) and adopting $n_{\rm H} = 2.8 \times 10^3$ cm^{-3} from the non-LTE analysis of CO, we get $\zeta \gtrsim 2.7 \times 10^{-14}$ s^{-1}. This value is higher than the typical value in MCs (~10^{-17} s^{-1}; A. E. Glassgold & W. D. Langer 1974) by three orders of magnitude, and the values obtained in W51C and W28 with the same method by one order of magnitude (C. Ceccarelli et al. 2011; S. Vaupré et al. 2014).

We note, however, that chemical equilibrium is not necessarily reached in 3C391:NML. Although the timescale of gas-phase ion–neutral reactions induced by CRs is only ~10^2 yr (S. Vaupré et al. 2014), grain chemistry may take a longer time to reach equilibrium. The deuterium chemistry is strongly affected by grain processes (e.g., S. Feng et al. 2020). We recall that the rate coefficient of CR-induced non-thermal desorption for a specific grain species is (T. I. Hasegawa & E. Herbst 1993)

$$k_{\rm CR} = f(70\ {\rm K})k_{\rm des}(70\ {\rm K}), \quad (7)$$

where f(70 K) is the fraction of the time spent by dust grains at the dust temperature $T_{\rm dust} = 70$ K due to CR heating, which is approximately (L. Reboussin et al. 2014)

$$f(70\ {\rm K}) = \frac{\zeta}{1.3 \times 10^{-17}\ {\rm s}^{-1}} \times 3.16 \times 10^{-19}. \quad (8)$$

The value $k_{\rm des}$(70 K) is the rate coefficient of the thermal desorption at $T_{\rm dust} = 70$ K, which can be expressed as

$$k_{\rm des} = \nu_0 \exp\left(-\frac{E_{\rm D}}{kT_{\rm dust}}\right), \quad (9)$$

where $E_{\rm D}$ is the desorption energy of the adsorbed species, and

$$\nu_0 = \left(\frac{2n_{\rm s}E_{\rm D}}{\pi^2 m}\right)^{1/2}, \quad (10)$$

where $n_{\rm s} \sim 1.5 \times 10^{15}$ cm^{-2} is the surface density of sites and m is the mass of the adsorbed species. For CO, the desorption energy is ≈1200 K (T. I. Hasegawa & E. Herbst 1993). Substituting the values into these equations, we estimate that the CR-induced non-thermal desorption timescale for CO ice at $\zeta \sim 10^{-14}$ s^{-1} is $\tau_{\rm CR} \approx 1/k_{\rm CR} \sim 3 \times 10^3$ yr, which is comparable to the age of SNR 3C 391 (4–19 kyr; see our further discussion in Section 4.2.3). We note that $k_{\rm CR}$ depends exponentially on the desorption energy $E_{\rm D}$ (see Equation (9)), which varies with species. A substantial proportion of ice is composed of H_2O, NH_3, CH_3OH, etc. (M. Ruaud et al. 2016). These species have higher values of $E_{\rm D}$, which result in a longer desorption timescale. Therefore, the chemistry may be highly dynamic in the environment of 3C 391, and the CR ionization rate estimated with Equations (6) may thus deviate from the real value.

4.2.2. Unusual Abundance and Abundance Ratios Found by the Yebes Observation

Using the column densities listed in Table 2 and the estimated $N(H_2) \sim 5.8 \times 10^{21}$ cm^{-2}, we can obtain the abundances of the detected species. We find that the obtained $N(HCO^+)/N(HOC^+)$, $N(HCS^+)/N$(CS), and $X(l\text{-}C_3H^+)$ are different from typical values found in dense MCs. Here X denotes the abundance of a specific species relative to H_2. All of the three values can probably be attributed to the chemistry of CRs.

The observed value of $N(\mathrm{HCO^+})/N(\mathrm{HOC^+})$ is ∼160–180, while the typical value found in quiescent dense MCs in our Galaxy is $\sim 10^3$ (A. J. Apponi & L. M. Ziurys 1997), which is higher than our observed value by an order of magnitude. Low $N(\mathrm{HCO^+})/N(\mathrm{HOC^+})$ has been found in Galactic photodissociation regions (PDRs) (e.g., the Horsehead PDR (J. R. Goicoechea et al. 2009) and Orion Bar PDR (J. R. Goicoechea et al. 2017)), diffuse clouds (H. Liszt et al. 2004), and extragalactic sources (e.g., NGC 253 (N. Harada et al. 2021) and M 82 (A. Fuente et al. 2008)). In low-temperature molecular gas, N. Harada et al. (2021) proposed that the decrease in $N(\mathrm{HCO^+})/N(\mathrm{HOC^+})$ in gas with high visual extinction A_V shielded from UV radiation is caused by the extremely high CR ionization rate of $\sim 10^{-14}\ \mathrm{s^{-1}}$ in the central molecular zone (CMZ) of NGC 253. In this case, the reduction of $N(\mathrm{HCO^+})/N(\mathrm{HOC^+})$ is due to the enrichment of $\mathrm{C^+}$ and $\mathrm{CO^+}$, which in turn leads to a faster production of $\mathrm{HOC^+}$ through the reactions

$$\begin{aligned} \mathrm{C^+} + \mathrm{H_2O} &\longrightarrow \mathrm{HOC^+} + \mathrm{H} \\ &\longrightarrow \mathrm{HCO^+} + \mathrm{H} \end{aligned} \tag{11}$$

with a branching ratio of 2:1 (M. F. Jarrold et al. 1986), and

$$\begin{aligned} \mathrm{CO^+} + \mathrm{H_2} &\longrightarrow \mathrm{HOC^+} + \mathrm{H} \\ &\longrightarrow \mathrm{HCO^+} + \mathrm{H} \end{aligned} \tag{12}$$

with a branching ratio of approximately 1:1 (V. G. Anicich 1993).

The observed value of $N(\mathrm{HCS^+})/N(\mathrm{CS})$ is ∼0.14–0.18, while the typical values found in the Taurus, Perseus, and Orion MCs and the Barnard 1 dark cloud are all $\sim 10^{-2}$ (A. Fuente et al. 2016; M. Rodríguez-Baras et al. 2021), which is lower than our observed value by an order of magnitude. The chemical simulation of A. Fuente et al. (2016) shows that the enhanced $N(\mathrm{HCS^+})/N(\mathrm{CS})$ ratio could be a tracer of high CR ionization rate at chemical equilibrium, because $\mathrm{H_3^+}$, $\mathrm{HCO^+}$, and $\mathrm{H_3O^+}$, which are all important products of CR ionization, are important reactants that transform CS to $\mathrm{HCS^+}$ (L. Podio et al. 2014). However, this simulation considered only a narrow range of CR ionization rate and is limited to chemical equilibrium.

The observed value of $X(l\text{-}\mathrm{C_3H^+})$ is $\sim(3.1\text{–}6.0)\times 10^{-11}$. The l-$\mathrm{C_3H^+}$ molecular species was first discovered in the Horsehead PDR (J. Pety et al. 2012), and V. V. Guzmán et al. (2015) proposed that the high abundance of l-$\mathrm{C_3H^+}$ ($\sim 10^{-11}$) in the Horsehead is due to the PDR chemistry, which produces abundant $\mathrm{C^+}$ ions and possibly the photo-erosion of polycyclic aromatic hydrocarbons (PAHs). M. Gerin et al. (2019) found that l-$\mathrm{C_3H^+}$ is ubiquitous in diffuse gas, with an abundance of $\sim 7\times 10^{-11}$. The first detection of l-$\mathrm{C_3H^+}$ in a quiescent dense MC was reported by J. Cernicharo et al. (2022), who found $X(\mathrm{C_3H^+}) \sim 2.4\times 10^{-12}$ in the TMC-1 cloud. This value is lower than our observed value by an order of magnitude.

We note that the visual extinction of 3C391:NML is $A_V \approx 6.2$ assuming $N_{\mathrm{H}}/A_V = 1.87\times 10^{21}\ \mathrm{cm^{-2}\ mag^{-1}}$ (R. C. Bohlin et al. 1978). In addition, we do not find any source of strong UV radiation close to the MC in the SIMBAD database[15] (M. Wenger et al. 2000). Therefore, the chemistry of 3C391:NML is not likely to be dominated by UV photons (M. G. Wolfire et al. 2022). On the other hand, CRs, which can enhance the abundances of ionized species such as $\mathrm{C^+}$, $\mathrm{H_3^+}$, $\mathrm{CO^+}$, and $\mathrm{H_3O^+}$, may provide advantages to explain the observed abundance and abundance ratios.

4.2.3. Results of Chemical Simulation

To further investigate the chemistry and constrain the cosmic-ray ionization rate in 3C391:NML, we present a chemical simulation using the `DNautilus 2.0` chemical code (K. Taniguchi et al. 2024). This code represents an updated version of `DNAUTILUS.1.0` as introduced by L. Majumdar et al. (2017). It is capable of simulating time-dependent abundances in two phases (treating the entire grain as homogeneous) and three phases (making a distinction between the surface and bulk of the grain).

In `DNautilus 2.0`, deuteration is achieved up to the 14th largest atom-based molecule present in the kida.uva.2014 network, which is available in the KIDA database.[16] The deuteration routine used is described in T. Albertsson et al. (2013), resulting in 1606 gas species, 1472 grain-surface species, and 1472 grain-mantle species. These are connected by 83,715 gas-phase reactions, 10,967 reactions on grain surfaces, and 9431 reactions in the grain mantles in `DNautilus 2.0`.

The simulation consists of two steps. In step 1, we simulate the chemistry of a dense MC with low CR ionization rate per $\mathrm{H_2}$ ($\zeta = 10^{-17}\ \mathrm{s^{-1}}$) and low gas temperature $T = 10$ K for $t_1 = 0.1$ and 1 Myr to mimic the chemical evolution of the MC before the supernova explosion. A grid of density n_{H} (10 values between 2×10^3 and $2\times 10^6\ \mathrm{cm^{-3}}$) and C/O element ratio (0.6, 0.8, 1.0, and 1.2) is explored in step 1. Initially, all the abundances are in elemental form except for hydrogen and deuterium, which appear in molecular form as $\mathrm{H_2}$ and HD, respectively. Elements whose ionization potentials are less than 13.6 eV, such as C, S, Si, Fe, Na, Mg, Cl, and P, appear in their first ionization states. In step 2, we use the results of step 1 as input abundances, keep the density and the C/O ratio constant, and vary ζ (10^{-17}, 10^{-16}, 10^{-15}, and $10^{-14}\ \mathrm{s^{-1}}$) and T (10 values between 10 and 50 K) to mimic the impact of CRs after the supernova explosion. We note that the CR ionization rate has non-negligible influence on the temperature of molecular gas (P. F. Goldsmith & W. D. Langer 1978). However, it is hard to determine the exact values of gas temperature at different CR ionization rates analytically, and different calculations give different results (e.g., E. Bayet et al. 2011; T. G. Bisbas et al. 2017). Therefore, we set these two parameters to be independent and fix the temperature throughout step 2. Throughout the simulation, the cloud is assumed to be shielded from incident UV. But the secondary UV photons generated by CR radiation are considered, with 10^4 secondary photons per CR field of $1.3\times 10^{-17}\ \mathrm{s^{-1}}$ (C. J. Shen et al. 2004). The physical parameters that are explored are listed in Table 3. The initial elemental abundances for step 1 are shown in Table 4 and the initial abundances of $\mathrm{H_3^+}$, $\mathrm{H_2D^+}$, $\mathrm{HCO^+}$, $\mathrm{DCO^+}$, and CO for step 2 for the C/O ratio 0.8 in Table 5.

The evolution time for step 2 is chosen according to the age of 3C 391. With various scenarios such as Sedov evolution, cloud evaporation, and radiative phase, the age of SNR 3C 391 was estimated within the range between 4 and 19 kyr (S. P. Reynolds & D. A. Moffett 1993; J.-H. Rho & R. Petre 1996; Y. Chen & P. O. Slane 2001; Y. Chen et al. 2004; D. A. Leahy & S. Ranasinghe 2018). We extract the abundances of the species in step 2 at 8000 yr, which is an intermediate value. The results of the simulation are shown in Figure 5 for both $t_1 = 0.1$ and 1 Myr. We note that the

---

[15] https://simbad.u-strasbg.fr/simbad/

[16] https://kida.astrochem-tools.org/

Table 3
Physical Parameters for Step 1 and Step 2

Parameter	Value Used in Step 1	Value Used in Step 2
t_1 (Myr)	0.1, 1	…
T (K)	10	10–50
n_H (cm^{-3})	2×10^3–2×10^6	2×10^3–2×10^6
$\log_{10}(\zeta/s^{-1})$	−17	−17, −16, −15, −14
C/O ratio	0.6, 0.8, 1.0, 1.2	0.6, 0.8, 1.0, 1.2

Table 4
Initial Elemental Abundances for Step 1

Element	Abundance Relative to H
H_2	0.50
He	9.00(−2)
N	6.20(−5)
O	(2.83, 2.12, 1.70, 1.41)(−4)
C^+	1.70(−4)
S^+	8.00(−8)
Si^+	8.00(−8)
Fe^+	3.00(−9)
Na^+	2.00(−9)
Mg^+	7.00(−9)
P^+	2.00(−10)
Cl^+	1.00(−9)
F	6.68(−9)
HD	1.60(−5)

difference in results with different C/O ratios is negligible. So we only show the results with C/O = 0.8 as a representative case in Figure 5. The difference between the results with $t_1 = 0.1$ and 1 Myr is due to the different levels of depletion in step 1, and thus the different initial conditions in step 2. Although the $N(HCO^+)/N(CO)$ abundance ratio can be used to estimate the CR ionization rate (Equation (6)), here we do not use it for our simulation because CO traces less dense gas than other species (see Section 4.1.1 and Y. L. Shirley 2015).

The simulation fails to reproduce the observed values of $N(HCS^+)/N(CS)$ (0.14–0.18), with typical simulated values $\lesssim 10^{-2}$ in any combination of parameters. We attempted to reproduce the observed $N(HCS+)/N(CS)$ ratios by assuming different initial sulfur abundances. However, all models do not match the observed values. This may result from some chemical effects of sulfur, for example, the form of sulfur depletion in dark MCs (T. H. G. Vidal et al. 2017), which are not considered in our chemical model. Due to this sulfur conundrum, we do not show the results here.

The two abundance ratios are both related to the HCO^+ molecule. The formation of HCO^+ is mainly through

$$CO + H_3^+ \longrightarrow HCO^+ + H_2 \tag{13}$$

in most of the physical conditions whereas the formation reactions of HOC^+ including reactions (11) and (12) depend on the specific values of ζ, n_H, and T. The major production and destruction pathways of HCO^+ and HOC^+ are listed in Table 6. We note that the abundance ratio $N(HCO^+)/N(HOC^+)$ exhibits a rather regular dependence on different physical parameters at $T \lesssim 40$ K—decreasing with higher ζ and lower n_H, while decreasing with higher T (not shown in Figure 5). We therefore propose that the low $N(HCO^+)/N(HOC^+)$ abundance ratio may be a good tracer of enhanced CR ionization rate in dark unshocked clouds associated with SNRs if other physical parameters are well constrained by observation.

The molecule l-C_3H^+, as a carbon chain species, is expected to be sensitive to the C/O ratio (e.g., P. Pratap et al. 1997). However, we find that the dependence of $X(l\text{-}C_3H^+)$ on the C/O ratio is not very significant, which is also reported by J.-C. Loison et al. (2014), and does not affect our conclusions. We note that the $X(l\text{-}C_3H^+)$ is higher when the CR ionization rate is higher.

In general, we find that four combinations of parameters can reproduce the three observed values: (1) $t_1 = 0.1$ Myr, $n_H \sim 10^{3.5}$ cm^{-3}, $T \sim 50$ K, $\zeta \sim 10^{-17}$ s^{-1}; (2) $t_1 = 0.1$ Myr, $n_H \sim 10^4$ cm^{-3}, $T \sim 35$ K, $\zeta \sim 10^{-16}$ s^{-1}; (3) $n_H \sim 10^4$ cm^{-3}, $T \sim 35$ K, $\zeta \sim 10^{-15}$ s^{-1}; and (4) $n_H \sim 10^5$ cm^{-3}, $T \sim 40$ K, $\zeta \sim 10^{-14}$ s^{-1}. Combinations 1 and 2 are only valid for $t_1 = 0.1$ Myr, while 3 and 4 are valid for both values of t_1. The densities in all the four combinations are within the range obtained from our non-LTE analysis of CO, o-c-C_3H_2, and CS (see Section 4.1.1).

However, as we have mentioned above, the gas temperature is dependent on the CR ionization rate because of the heating effect of CRs. The calculation of E. Bayet et al. (2011) shows that the gas temperatures are ∼10, ∼20, ∼40, and ∼80 K for $\zeta \sim 10^{-17}$, 10^{-16}, 10^{-15}, and 10^{-14} s^{-1}, respectively, while T. G. Bisbas et al. (2017) predict ∼10, ∼10, ∼20, and ∼40 K correspondingly. Comparing these values with our simulation results, we find that combinations 1 and 2 are not compatible with the CR heating as they require higher temperatures than the values predicted by E. Bayet et al. (2011) and T. G. Bisbas et al. (2017), while the slightly elevated temperatures in combinations 3 and 4 can be naturally explained by CR heating.

We note that SNR 3C 391 is a bright source in X-rays, which can penetrate deeper into MCs than UV photons (M. G. Wolfire et al. 2022) and can heat the molecular gas deep inside them. To evaluate whether X-rays can provide the required heating for combinations 1 and 2, we here estimate and compare the heating rates of X-rays and CRs. For X-ray emission with a photon index α, the X-ray heating rate per unit volume is (P. R. Maloney et al. 1996)

$$\Gamma_X \approx 3 \times 10^4 \left(\frac{f_h}{0.3}\right)\left(\frac{n_H}{10^5\ \mathrm{cm}^{-3}}\right) H_X \tag{14}$$

where $f_h \approx 0.3$ is the fraction of primary photoelectron energy that goes into gas heating, and

$$H_X \approx \frac{3\sigma_0 C_\alpha F_X}{8\tau_1^{\phi+1}} S(\tau_1), \tag{15}$$

where $\sigma_0 = 2.6 \times 10^{-22}$ cm^2, $C_\alpha = (1 - \alpha)/(E_{k,\max}^{1-\alpha} - E_{k,\min}^{1-\alpha})$ for $\alpha \neq 1$, $E_{k,\min}$ and $E_{k,\max}$ are the minimum and maximum energies in units of keV, F_X is the X-ray flux at the target point, $\phi = 3(\alpha - 1)/8$, the optical depth at 1 keV from the X-ray source to 3C391:NML is $\tau_1 = 2.6 N_{22}$, and $S(\tau_1) \approx 1$ for $10^{-2} \lesssim \tau_1 \lesssim 10^4$. For 3C 391, the X-ray luminosity is 2.3×10^{36} erg s^{-1} in 0.5–10 keV, and the mean distance between 3C 391 and 3C391:NML is 7 pc (Y. Chen et al. 2004). The attenuating column density N_H is assumed to be 10^{22} cm^{-2} so that $N_{22} = 1$. We note that Γ_X depends on the X-ray photon index α, but the X-ray spectrum of 3C 391 is dominated by a thermal component that cannot be fitted simply

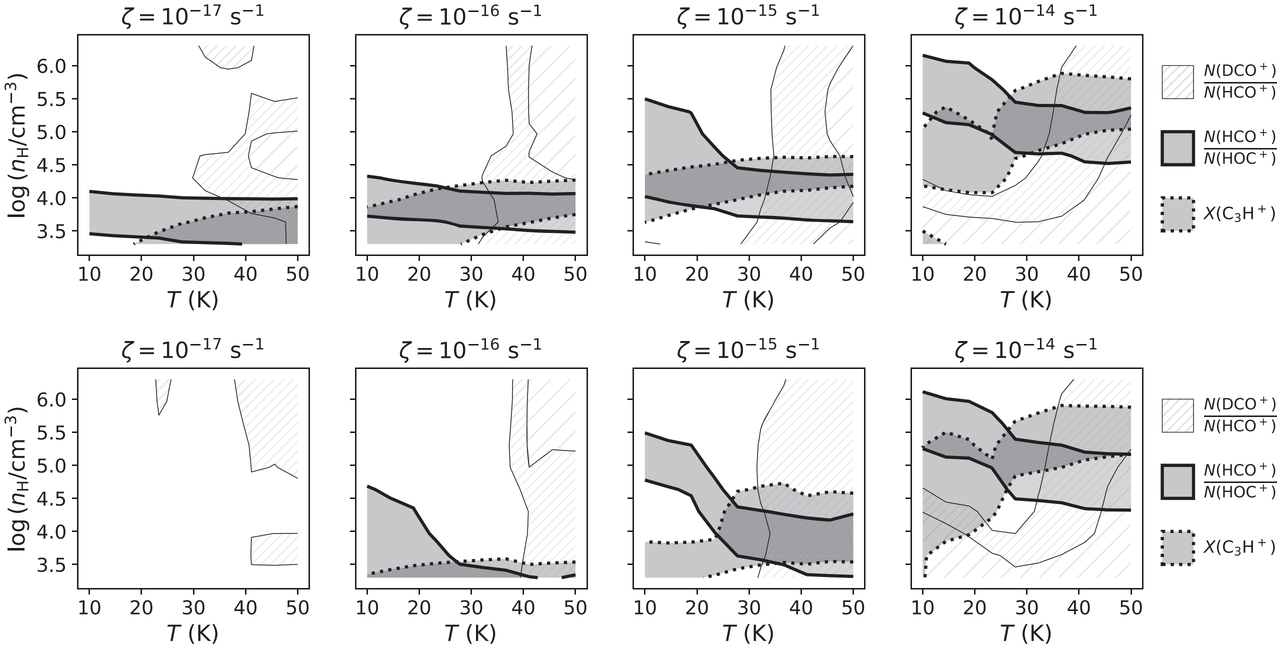

Figure 5. Results of the chemical simulation for $N(\mathrm{DCO}^+)/N(\mathrm{HCO}^+)$, $N(\mathrm{HCO}^+)/N(\mathrm{HOC}^+)$, and $X(l\text{-}\mathrm{C_3H}^+)$ with $t_1 = 0.1$ Myr (upper panel) and 1 Myr (lower panel) and C/O = 0.8. Each column shows the results with fixed ζ (CR ionization rate per H_2) from 10^{-17} to $10^{-14}\ \mathrm{s}^{-1}$. The hatched and shaded regions show the combinations of parameters that can reproduce the observational results within a factor of 2. As denoted in the labels on the right, the densely hatched regions with solid thin bounds show $N(\mathrm{DCO}^+)/N(\mathrm{HCO}^+)$ (while the sparsely hatched regions mean that the modeled $N(\mathrm{DCO}^+)/N(\mathrm{HCO}^+)$ is lower than half of the estimated upper limits obtained from observation), the shaded regions with solid thick bounds show $N(\mathrm{HCO}^+)/N(\mathrm{HOC}^+)$, and the shaded regions with dotted bounds show $X(l\text{-}\mathrm{C_3H}^+)$.

Table 5
Relative Abundance of Some Molecules with Respect to H for Step 2 for C/O Ratio = 0.8

t_1 (Myr)	n_H (cm^{-3})	H_3^+	$\mathrm{H_2D}^+$	HCO^+	DCO^+	CO
0.1	2×10^3	2.41(−9)	7.70(−11)	1.53(−9)	1.50(−11)	3.28(−5)
	2×10^4	2.59(−10)	1.17(−11)	3.55(−10)	2.67(−12)	4.62(−5)
	2×10^5	7.58(−10)	8.55(−10)	8.96(−11)	1.26(−10)	4.11(−7)
	2×10^6	2.14(−10)	2.89(−10)	1.85(−12)	2.94(−12)	7.90(−9)
1.0	2×10^3	4.90(−9)	3.02(−10)	7.55(−9)	2.10(−10)	7.34(−5)
	2×10^4	7.20(−9)	2.88(−9)	4.72(−10)	1.34(−10)	1.27(−6)
	2×10^5	4.07(−9)	1.14(−9)	3.76(−11)	5.29(−12)	7.50(−8)
	2×10^6	1.36(−9)	3.39(−10)	3.98(−12)	3.76(−13)	7.57(−9)

Table 6
Major Chemical Reactions for HCO^+, HOC^+, DCO^+, and CO

Species	Production Reactions	Destruction Reactions
HCO^+	$\mathrm{CO} + \mathrm{H}_3^+ \rightarrow \mathrm{H}_2 + \mathrm{HCO}^+$	$\mathrm{HCO}^+ + e^- \rightarrow \mathrm{H} + \mathrm{CO}$ $\mathrm{HCN} + \mathrm{HCO}^+ \rightarrow \mathrm{CO} + \mathrm{HCNH}^+$ ($\zeta \lesssim 10^{-16}\ \mathrm{s}^{-1}$ and $T \gtrsim 43$ K)
HOC^+	$\mathrm{CO} + \mathrm{H}_3^+ \rightarrow \mathrm{H}_2 + \mathrm{HOC}^+$ $\mathrm{H_2O} + \mathrm{C}^+ \rightarrow \mathrm{H} + \mathrm{HOC}^+$ ($n_\mathrm{H} \lesssim 2\times10^4\ \mathrm{cm}^{-3}$) $\mathrm{H}_2 + \mathrm{CO}^+ \rightarrow \mathrm{H} + \mathrm{HOC}^+$	$\mathrm{HOC}^+ + \mathrm{H}_2 \rightarrow \mathrm{HCO}^+ + \mathrm{H}_2$ $\mathrm{HOC}^+ + e^- \rightarrow \mathrm{H} + \mathrm{CO}$ ($n_\mathrm{H} \approx 2\times10^3\ \mathrm{cm}^{-3}$)
DCO^+	$\mathrm{HCO}^+ + \mathrm{D} \rightarrow \mathrm{DCO}^+ + \mathrm{H}$ $\mathrm{CO} + \mathrm{CH_4D}^+ \rightarrow \mathrm{CH}_4 + \mathrm{DCO}^+$	$\mathrm{DCO}^+ + \mathrm{HCN} \rightarrow \mathrm{HDCN}^+ + \mathrm{CO}$ ($T \gtrsim 43$ K) $\mathrm{DCO}^+ + e^- \rightarrow \mathrm{D} + \mathrm{CO}$
CO	$\mathrm{HCO}^+ + e^- \rightarrow \mathrm{CO} + \mathrm{H}$ $\mathrm{CO_{ice}} \rightarrow \mathrm{CO}$ ($T \gtrsim 23$ K)	$\mathrm{CO} + \mathrm{H}_3^+ \rightarrow \mathrm{H}_2 + \mathrm{HCO}^+$ $\mathrm{CO} \rightarrow \mathrm{CO_{ice}}$ ($T \gtrsim 23$ K) $\mathrm{CO} + \mathrm{He}^+ \rightarrow \mathrm{He} + \mathrm{O} + \mathrm{C}^+$

with a power law. Assuming $\alpha \approx 3.3$, which is adopted by P. Zhou et al. (2018) in SNR Cas A, and $n_\mathrm{H} = 10^4\ \mathrm{cm}^{-3}$, we get $\Gamma_\mathrm{X} \sim 4\times10^{-27}\ \mathrm{erg\ cm^{-3}\ s^{-1}}$. Changing the value of α does not affect the basic conclusion that $\Gamma_\mathrm{X} < 10^{-26}\ \mathrm{erg\ cm^{-3}\ s^{-1}}$.

For the heating rate of CRs, we adopt the equations in P. F. Goldsmith & W. D. Langer (1978) and the assumptions in P. Zhou et al. (2018):

$$\Gamma_\mathrm{CR} \approx 3.2\times10^{-25}\left(\frac{n_{\mathrm{H}_2}}{10^3\ \mathrm{cm}^{-3}}\right) \times \left(\frac{\zeta}{10^{-17}\ \mathrm{s}^{-1}}\right)\ \mathrm{erg\ cm^{-3}\ s^{-1}}. \tag{16}$$

For combinations 1 and 2 in our simulation, we get $\Gamma_\mathrm{CR} \approx 10^{-24}$ and $2\times10^{-23}\ \mathrm{erg\ cm^{-3}\ s^{-1}}$, respectively, which are significantly higher than the X-ray heating rate. Considering that there is no evidence of other heating sources such as star formation activity (J. S. Urquhart et al. 2018), shocks (introduced in Section 1), and external UV radiation (discussed in Section 4.2.2), we suggest that combinations 1 and 2 cannot be used to reproduce the observation.

For combinations 3 and 4, gas temperatures of ∼35 and ∼40 K are required. Due to the large scatter in the relation between T and the line ratio $I(\mathrm{H^{13}CN})/I(\mathrm{HN^{13}C})$ (A. G. Pazukhin et al. 2022) and the uncertainty in the non-LTE analysis in Section 4.1.1 (for example, the unknown spatial distribution of the molecular gas inside the telescope beam), the moderately enhanced temperatures in combinations 3 and 4 are indeed possible. Adopting a temperature of 40 K does not result in a significant change in the molecular column densities (see Section 4.1.1). In conclusion, an enhanced CR ionization rate ($\sim 10^{-15}$ or $10^{-14}\ \mathrm{s^{-1}}$) is required to reproduce the observation according to the simulation.

4.3. Enhanced CR Ionization Rate Associated with SNR 3C 391

In the previous section, we find an enhanced CR ionization rate associated with SNR 3C 391. However, X-rays can also induce chemistry similar to CRs (S. Viti 2017). Y. Chen et al. (2004) found that the X-ray ionization rate of the position toward an 1720 MHz OH maser that is close to 3C391:NML (see Figure 1) is $\zeta_{\mathrm{X}} \sim 2 \times 10^{-15}\ \mathrm{s^{-1}}$, but their estimation may overestimate the X-ray ionization rate because the equation assumes the X-ray spectrum comprises only photons of 1 keV (M. Wardle 1999), which have the strongest ionization effect. For a more realistic consideration, we adopt the equations in P. R. Maloney et al. (1996):

$$\zeta_{\mathrm{X}} \approx 1.83 \times 10^{10} \frac{f_i}{0.4} H_{\mathrm{X}}, \tag{17}$$

where $f_i \approx 0.4$ is the fraction of primary photoelectron energy that goes into ionization and H_{X} has been defined in Equation (15). Based on the assumptions in the previous section, we get $\zeta_{\mathrm{X}} \sim 3 \times 10^{-20}\ \mathrm{s^{-1}}$, which is significantly lower than the CR ionization rate. Changing the value of α does not affect the basic conclusion that $\zeta_{\mathrm{X}} < 10^{-19}\ \mathrm{s^{-1}}$. Although this is just a rough estimation of the order of magnitude of ζ_{X}, we conclude that the chemistry in 3C391:NML is dominated by CRs instead of X-ray photons.

The obtained CR ionization rate, $\zeta \sim 10^{-15}$ or $10^{-14}\ \mathrm{s^{-1}}$, is ∼2–3 orders of magnitude higher than typical values in MCs (A. E. Glassgold & W. D. Langer 1974; P. Caselli et al. 1998). The CR ionization rate of $\sim 10^{-15}\ \mathrm{s^{-1}}$ is similar to the values found in MCs associated with SNRs W51C (C. Ceccarelli et al. 2011) and W28 (S. Vaupré et al. 2014). If $\zeta \sim 10^{-14}\ \mathrm{s^{-1}}$ is true, this is even higher by an order of magnitude than the values in MCs associated with other SNRs. This extremely high value of CR ionization rate has been found in the CMZ of our Galaxy (e.g., T. Oka et al. 2019), the solar-type protostar OMC-2 FIR4 (C. Ceccarelli et al. 2014; F. Fontani et al. 2017), and CMZs of other galaxies such as NGC 253 (J. Holdship et al. 2022). The origin of the extremely high CR ionization rate in the CMZ of our Galaxy arises from a combination of energetic activities including SNRs and colliding winds of massive stars (e.g., F. Yusef-Zadeh et al. 2007), whereas V. Lattanzi et al. (2023) proposed that the high CR ionization rate in OMC-2 FIR4 is due to CRs accelerated in the jet shock of the young protostar. However, no star formation activity is found to be associated with 3C391:NML (J. S. Urquhart et al. 2018). Therefore, it is more likely that the extremely high ζ obtained in 3C391:NML originates from the SNR. Extrapolating the high-energy CR spectrum inferred from the γ-ray observation to low energies, F. Schuppan et al. (2012) found that SNR 3C 391 can induce $\zeta \sim 10^{-14}\ \mathrm{s^{-1}}$ in its surrounding MCs. According to their calculation, a possible reason why 3C 391 can induce a higher CR ionization rate than other SNRs is that the deduced proton flux of 3C 391 at <1 GeV is higher than those of other SNRs, which means the MCs adjacent to 3C 391 are exposed to more ionizing low-energy CR protons. Yet this extrapolation is not exempt from problems, because the CRs leading to ionization have too low an energy ($\lesssim$280 MeV, M. Padovani et al. 2009) to produce γ-ray emission detectable by available instruments.

5. Conclusion

In this paper, we performed a W-band (71.5–90 GHz) line survey with the Yebes 40 m radio telescope toward an unshocked molecular cloud of SNR 3C 391, which we call 3C391:NML. Our main conclusions are summarized as follows.

1. We detected 18 molecules in the line survey. The line profile of the $\mathrm{HCO^+}$ $J = 1$–0 line exhibits three components with different line-widths, while most molecular lines only exhibit a narrow component and some exhibit two components.
2. Assuming $T = 20$ K, we estimated the physical parameters of 3C391:NML using the SpectralRadex code with the CO, o-c-$\mathrm{C_3H_2}$, and CS lines. The density is estimated to be $n_{\mathrm{H_2}} \sim 1.4 \times 10^3\ \mathrm{cm^{-3}}$ from the CO lines, and $\sim 2 \times 10^5\ \mathrm{cm^{-3}}$ from the o-c-$\mathrm{C_3H_2}$ and CS lines. The estimated $N_{\mathrm{H_2}}$ of the MC is $\sim 5.8 \times 10^{21}\ \mathrm{cm^{-2}}$.
3. Using the analytic equations reported by S. Vaupré et al. (2014), we estimated the CR ionization rate of 3C391:NML is $\gtrsim 2.7 \times 10^{-14}\ \mathrm{s^{-1}}$ with the abundance ratio $N(\mathrm{HCO^+})/N(\mathrm{CO})$ and an upper limit of $N(\mathrm{DCO^+})/N(\mathrm{HCO^+})$. However, we caution on adopting this value because chemical equilibrium, which is a prerequisite of using the equations, is not necessarily reached in the MC considering the 4–19 kyr age of 3C 391.
4. We found some unusual abundances and abundance ratios compared with typical values in quiescent dense MCs. They are: $N(\mathrm{HCO^+})/N(\mathrm{HOC^+}) \sim 160$–180 lower than typical values, $N(\mathrm{HCS^+})/N(\mathrm{CS}) \sim 0.14 - 0.18$ higher than typical values, and $X(l\text{-}\mathrm{C_3H^+}) \sim (3.1\text{–}6.0) \times 10^{-11}$ higher than typical values by an order of magnitude. These can be attributed to the chemistry induced by CRs.
5. Using the `DNautilus 2.0` chemical model equipped with deuterium chemistry, we present a chemical simulation to explain the observed abundances and abundance ratios. We found that two combinations of parameters can reproduce the observation: $n_{\mathrm{H}} \sim 10^4\ \mathrm{cm^{-3}}$, $T \sim 35$ K, $\zeta \sim 10^{-15}\ \mathrm{s^{-1}}$ and $n_{\mathrm{H}} \sim 10^5\ \mathrm{cm^{-3}}$, $T \sim 40$ K, $\zeta \sim 10^{-14}\ \mathrm{s^{-1}}$. The moderately elevated temperatures can be naturally explained by CR heating. The obtained CR ionization rate is higher than typical values in MCs by 2–3 orders of magnitude. If $\zeta \sim 10^{-14}\ \mathrm{s^{-1}}$ is true, this is higher than those in MCs associated with other SNRs by an order of magnitude, which may be because 3C 391 is exposed to more ionizing low-energy CR protons than other SNRs.

Acknowledgments

T.-Y. T. thanks Siyi Feng, Thomas Bisbas, Yichen Sun, and Xiao Zhang for their helpful discussions. L.M. acknowledges the financial support of DAE and DST-SERB research grants (SRG/2021/002116 and MTR/2021/000864) of the Government of India. Y.C. acknowledges the support from NSFC grants Nos. 12173018, 12121003, and 12393852. P.Z. acknowledges the support from NSFC grant No. 12273010. M. S.-G. has carried out the observations and the first inspection of the data quality.

This article is based on observations carried out with the Yebes 40 m telescope (project code: 23A021). The 40 m radio telescope at Yebes Observatory is operated by the Spanish Geographic Institute (IGN; Ministerio de Transportes, Movilidad y Agenda Urbana). This research has also made use of the SIMBAD database, operated at CDS, Strasbourg, France.

Software: astropy (Astropy Collaboration et al. 2018, 2022), Spectral-cube (A. Ginsburg et al. 2015), GILDAS (Gildas Team, https://www.iram.fr/IRAMFR/GILDAS/), Montage (http://montage.ipac.caltech.edu/), Matplotlib (https://matplotlib.org).

Appendix A
Full Spectrum

In Figures 6 and 7 we show the entire spectrum in 71.5–90 GHz of our observation to show the full result of the line survey.

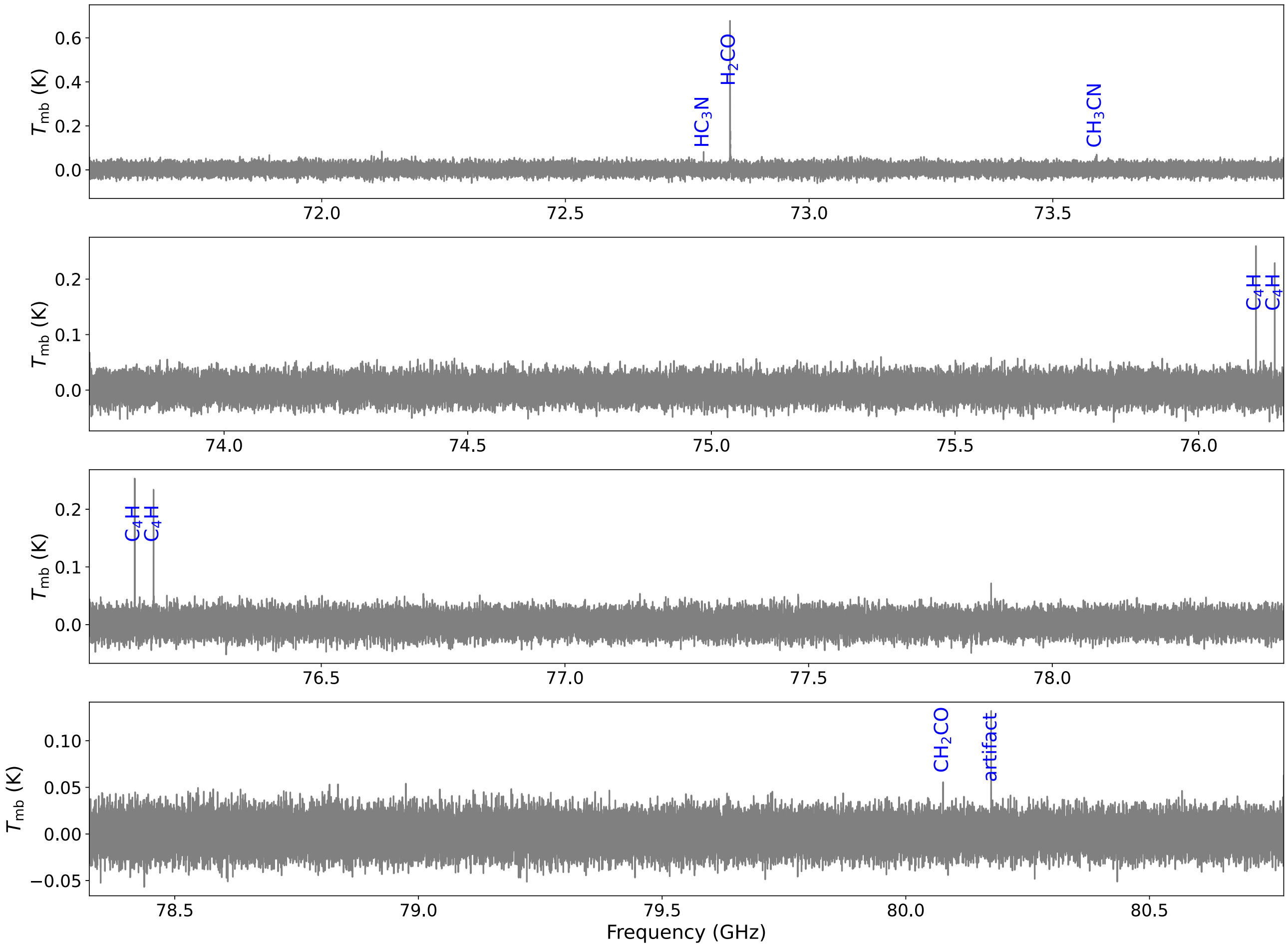

Figure 6. Full spectrum in the entire frequency range covered by eight spectrometers. Every two adjacent spectrometers have overlaps in frequency. The detected species and strong artifacts are marked in blue.

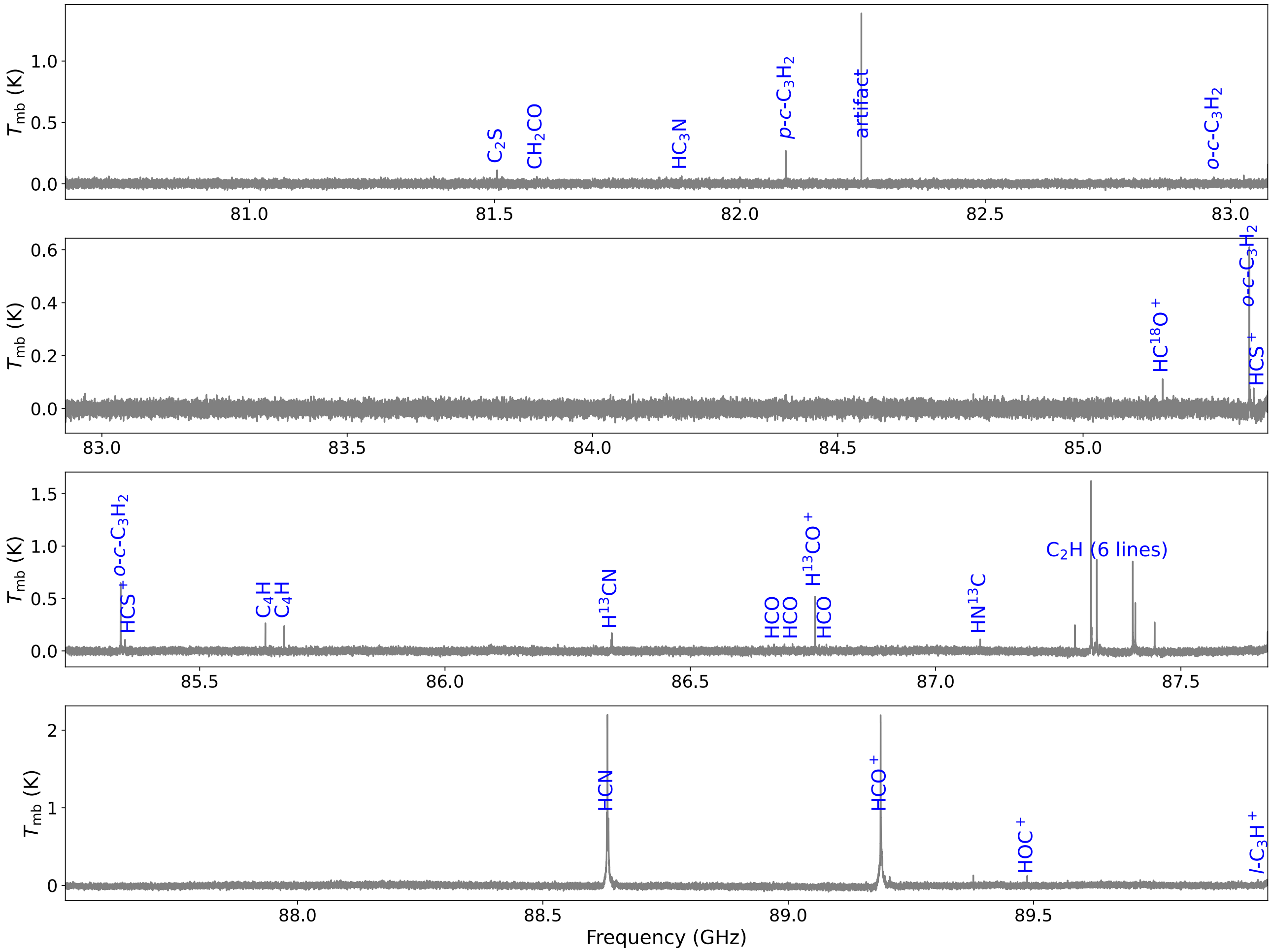

Figure 7. Continued.

ORCID iDs

Tian-Yu Tu (涂天宇) https://orcid.org/0000-0002-9776-5610
Prathap Rayalacheruvu https://orcid.org/0009-0001-6483-7366
Liton Majumdar https://orcid.org/0000-0001-7031-8039
Yang Chen (陈阳) https://orcid.org/0000-0002-4753-2798
Ping Zhou (周平) https://orcid.org/0000-0002-5683-822X
Miguel Santander-García https://orcid.org/0000-0002-7338-0986

References

Aharonian, F. A. 2013, APh, 43, 71
Albertsson, T., Semenov, D. A., Vasyunin, A. I., Henning, T., & Herbst, E. 2013, ApJS, 207, 27
Anicich, V. G. 1993, JPCRD, 22, 1469
Apponi, A. J., & Ziurys, L. M. 1997, ApJ, 481, 800
Astropy Collaboration, Price-Whelan, A. M., Lim, P. L., et al. 2022, ApJ, 935, 167
Astropy Collaboration, Price-Whelan, A. M., Sipőcz, B. M., et al. 2018, ApJ, 156, 123
Bayet, E., Williams, D. A., Hartquist, T. W., & Viti, S. 2011, MNRAS, 414, 1583
Bisbas, T. G., van Dishoeck, E. F., Papadopoulos, P. P., et al. 2017, ApJ, 839, 90
Bohlin, R. C., Savage, B. D., & Drake, J. F. 1978, ApJ, 224, 132
Caselli, P., Walmsley, C. M., Terzieva, R., & Herbst, E. 1998, ApJ, 499, 234
Ceccarelli, C., Dominik, C., López-Sepulcre, A., et al. 2014, ApJ, 790, L1
Ceccarelli, C., Hily-Blant, P., Montmerle, T., et al. 2011, ApJ, 740, L4
Cernicharo, J., Agúndez, M., Cabezas, C., et al. 2022, A&A, 657, L16
Chen, Y., & Slane, P. O. 2001, ApJ, 563, 202
Chen, Y., Su, Y., Slane, P. O., & Wang, Q. D. 2004, ApJ, 616, 885
Cosentino, G., Jiménez-Serra, I., Caselli, P., et al. 2019, ApJ, 881, L42
Ergin, T., Sezer, A., Saha, L., et al. 2014, ApJ, 790, 65
Feng, S., Li, D., Caselli, P., et al. 2020, ApJ, 901, 145
Ferrand, G., & Safi-Harb, S. 2012, AdSpR, 49, 1313
Fontani, F., Ceccarelli, C., Favre, C., et al. 2017, A&A, 605, A57
Frail, D. A., Goss, W. M., Reynoso, E. M., et al. 1996, ApJ, 111, 1651
Frerking, M. A., Langer, W. D., & Wilson, R. W. 1982, ApJ, 262, 590
Fuente, A., Cernicharo, J., Roueff, E., et al. 2016, A&A, 593, A94
Fuente, A., García-Burillo, S., Usero, A., et al. 2008, A&A, 492, 675
Gerin, M., Liszt, H., Neufeld, D., et al. 2019, A&A, 622, A26
Ginsburg, A., Robitaille, T., Beaumont, C., et al. 2015, in ASP Conf. Ser. 499 (San Francisco, CA: ASP), 363
Glassgold, A. E., & Langer, W. D. 1974, ApJ, 193, 73
Goicoechea, J. R., Cuadrado, S., Pety, J., et al. 2017, A&A, 601, L9
Goicoechea, J. R., Pety, J., Gerin, M., Hily-Blant, P., & Le Bourlot, J. 2009, A&A, 498, 771
Goldsmith, P. F., & Langer, W. D. 1978, ApJ, 222, 881
Guzmán, V. V., Pety, J., Goicoechea, J. R., et al. 2015, ApJ, 800, L33
Harada, N., Martín, S., Mangum, J. G., et al. 2021, ApJ, 923, 24
Hasegawa, T. I., & Herbst, E. 1993, MNRAS, 261, 83
Holdship, J., Mangum, J. G., Viti, S., et al. 2022, ApJ, 931, 89
Jarrold, M. F., Bowers, M. T., Defrees, D. J., McLean, A. D., & Herbst, E. 1986, ApJ, 303, 392
Jiang, B., Chen, Y., Wang, J., et al. 2010, ApJ, 712, 1147
Lattanzi, V., Alves, F. O., Padovani, M., et al. 2023, A&A, 671, A35
Leahy, D. A., & Ranasinghe, S. 2018, ApJ, 866, 9
Linsky, J. L., Draine, B. T., Moos, H. W., et al. 2006, ApJ, 647, 1106
Liszt, H., Lucas, R., & Black, J. H. 2004, A&A, 428, 117
Liu, X. C., Wu, Y., Zhang, C., et al. 2021, ApJ, 912, 148
Loison, J.-C., Wakelam, V., Hickson, K. M., Bergeat, A., & Mereau, R. 2014, MNRAS, 437, 930

Majumdar, L., Gratier, P., Ruaud, M., et al. 2017, MNRAS, 466, 4470
Maloney, P. R., Hollenbach, D. J., & Tielens, A. G. G. M. 1996, ApJ, 466, 561
Mangum, J. G., & Shirley, Y. L. 2015, PASA, 127, 266
Milam, S. N., Savage, C., Brewster, M. A., Ziurys, L. M., & Wyckoff, S. 2005, ApJ, 634, 1126
Nesterenok, A. V. 2022, MNRAS, 509, 4555
Oka, T., Geballe, T. R., Goto, M., et al. 2019, ApJ, 883, 54
Padovani, M., Galli, D., & Glassgold, A. E. 2009, A&A, 501, 619
Park, G., Currie, M. J., Thomas, H. S., et al. 2023, ApJS, 264, 16
Paulive, A., Carder, J. T., & Herbst, E. 2022, MNRAS, 516, 4097
Paulive, A., Shingledecker, C. N., & Herbst, E. 2021, MNRAS, 500, 3414
Pazukhin, A. G., Zinchenko, I. I., Trofimova, E. A., & Henkel, C. 2022, ARep, 66, 1302
Pety, J., Gratier, P., Guzmán, V., et al. 2012, A&A, 548, A68
Podio, L., Lefloch, B., Ceccarelli, C., Codella, C., & Bachiller, R. 2014, A&A, 565, A64
Prasad, S. S., & Tarafdar, S. P. 1983, ApJ, 267, 603
Pratap, P., Dickens, J. E., Snell, R. L., et al. 1997, ApJ, 486, 862
Ranasinghe, S., & Leahy, D. 2022, ApJ, 940, 63
Reach, W. T., & Rho, J. 1996, A&A, 315, L277
Reach, W. T., & Rho, J. 1998, ApJ, 507, L93
Reach, W. T., & Rho, J. 1999, ApJ, 511, 836
Reach, W. T., & Rho, J. 2000, ApJ, 544, 843
Reboussin, L., Wakelam, V., Guilloteau, S., & Hersant, F. 2014, MNRAS, 440, 3557
Reynolds, S. P., & Moffett, D. A. 1993, AJ, 105, 2226
Rho, J.-H., & Petre, R. 1996, ApJ, 467, 698
Rodríguez-Baras, M., Fuente, A., Riviére-Marichalar, P., et al. 2021, A&A, 648, A120
Ruaud, M., Wakelam, V., & Hersant, F. 2016, MNRAS, 459, 3756
Sato, T., Koyama, K., Takahashi, T., Odaka, H., & Nakashima, S. 2014, PASJ, 66, 124
Schuppan, F., Becker, J. K., Black, J. H., & Casanova, S. 2012, A&A, 541, A126
Shen, C. J., Greenberg, J. M., Schutte, W. A., & van Dishoeck, E. F. 2004, A&A, 415, 203
Shingledecker, C. N., Tennis, J., Gal, R. L., & Herbst, E. 2018, ApJ, 861, 20
Shirley, Y. L. 2015, PASP, 127, 299
Spitzer, L. 1978, Physical Processes in the Interstellar Medium (Weinheim: Wiley-VCH)
Sternberg, A., Dalgarno, A., & Lepp, S. 1987, ApJ, 320, 676
Taniguchi, K., Rayalacheruvu, P., Yonetsu, T., et al. 2024, ApJ, 963, 12
Tu, T.-y., Chen, Y., Zhou, P., Safi-Harb, S., & Liu, Q.-C. 2024, ApJ, 966, 178
Umemoto, T., Minamidani, T., Kuno, N., et al. 2017, PASJ, 69, 78
Urquhart, J. S., König, C., Giannetti, A., et al. 2018, MNRAS, 473, 1059
van der Tak, F. F. S., Black, J. H., Schöier, F. L., Jansen, D. J., & van Dishoeck, E. F. 2007, A&A, 468, 627
van der Tak, F., Lique, F., Faure, A., Black, J., & van Dishoeck, E. 2020, Atoms, 8, 15
Vaupré, S., Hily-Blant, P., Ceccarelli, C., et al. 2014, A&A, 568, A50
Vidal, T. H. G., Loison, J.-C., Jaziri, A. Y., et al. 2017, MNRAS, 469, 435
Viti, S. 2017, A&A, 607, A118
Wakelam, V., Dartois, E., Chabot, M., et al. 2021, A&A, 652, A63
Wardle, M. 1999, ApJ, 525, L101
Wenger, M., Ochsenbein, F., Egret, D., et al. 2000, A&AS, 143, 9
Wolfire, M. G., Vallini, L., & Chevance, M. 2022, ARA&A, 60, 247
Yan, Y. T., Henkel, C., Kobayashi, C., et al. 2023, A&A, 670, A98
Yusef-Zadeh, F., Muno, M., Wardle, M., & Lis, D. C. 2007, ApJ, 656, 847
Zhou, P., Li, J.-T., Zhang, Z.-Y., et al. 2018, ApJ, 865, 6
Zhou, P., Zhang, G.-Y., Zhou, X., et al. 2022, ApJ, 931, 144